Enhancing Optical, Electronic, Crystalline, and Morphological Properties of Cesium Lead Halide by Mn Substitution for?High-Stability All-Inorganic Perovskite Solar Cells with?Carbon Electrodes

doi: info:doi/10.1002/aenm.201800504

DOI: 10.1002/((please add manuscript number))
Article type: Communication

Enhancing Optical, Electronic, Crystalline, and Morphological Properties of Cesium Lead Halide by Mn Substitution for High-Stability All-Inorganic Perovskite Solar Cells with Carbon Electrodes

*Jia Liang, Zonghao Liu, Longbin Qiu, Zafer Hawash, Lingqiang Meng, Zhifang Wu, Yan Jiang, Luis K. Ono and Yabing Qi**

Dr. J. Liang, Dr. Z. Liu, Dr. L. Qiu, Dr. Z. Hawash, Dr. L. Meng, Dr. Z. Wu, Dr. Y. Jiang, D. L. Ono, Prof. Y. B. Qi
Energy Materials and Surface Sciences Unit (EMSSU)
Okinawa Institute of Science and Technology Graduate University (OIST)
1919-1 Tancha, Onna-son, Kunigami-gun, Okinawa 904-0495, Japan
E-mail: Yabing.Qi@OIST.jp
Dr. J. Liang
Department of Materials Science and NanoEngineering/Smalley-Curl Institute
Rice University
Houston, Texas 77005, USA

Keywords: doping, Mn, all-inorganic perovskite, perovskite solar cell, carbon electrode

In this work we dope all-inorganic perovskite $CsPbIBr_2$ with Mn to compensate their shortcomings in band structure for the application of perovskite solar cells (PSCs). The novel Mn-doped all-inorganic perovskites, $CsPb_{1-x}Mn_xI_{1+2x}Br_{2-2x}$, are prepared in ambient atmosphere. As the concentration of Mn^{2+} ions increases, the bandgaps of $CsPb_{1-x}Mn_xI_{1+2x}Br_{2-2x}$ decreases from 1.89 eV to 1.75 eV. Additionally, when the concentration of Mn dopants is appropriate, this novel Mn-doped all-inorganic perovskite film shows better crystallinity and morphology than the undoped counterpart. These advantages alleviate the energy loss in hole transfer and facilitate the charge-transfer in perovskites, therefore, PSCs based on these novel $CsPb_{1-x}Mn_xI_{1+2x}Br_{2-2x}$ perovskite films display better photovoltaic performances than the undoped $CsPbIBr_2$ perovskite films. The reference $CsPbIBr_2$ cell reached a PCE of 6.14%, comparable with the previous reports. The $CsPb_{1-x}Mn_xI_{1+2x}Br_{2-2x}$ cells reached the highest PCE of 7.36% (when x = 0.005), an increase of 19.9% in PCE. Furthermore, the encapsulated $CsPb_{0.995}Mn_{0.005}I_{1.01}Br_{1.99}$ cells exhibit good stability in ambient atmosphere. The storage

stability measurements on the encapsulated PSCs reveal that PCE dropped by only 8% of the initial value after >300 hours in ambient. Such improved efficiency and stability were achieved using low-cost carbon electrodes (without expensive HTMs and Au electrodes).

Perovskite solar cells (PSCs) have attracted a great deal of attention as they show promise toward the development of next generation solar cells.[1-18] Nowadays, the highest power conversion efficiency (PCE) has already reached to 22.7%.[19] Besides the commonly used organic ammonium based organic-inorganic perovskites, such as methylammonium lead iodide ($MAPbI_3$) and formamidinium lead iodide ($FAPbI_3$), the utilization of all-inorganic perovskites ($CsPbX_3$ (X = I, Br, and Cl)) is rising because they do not contain any volatile organic components and display much better thermal stability.[8-16] For example, $CsPbBr_3$, the most widely studied all-inorganic perovskite, showed excellent stability even under environmental stress without any encapsulation.[11-12] However, the light absorption for $CsPbBr_3$ is only up to ~540 nm, which limits the light harvesting capability. It is therefore desirable to tune the electronic and optical properties of all-inorganic perovskites to further enhance their photovoltaic performances.

Recent efforts to improve the PCEs of all-inorganic perovskites based PSCs include the replacement of Br^- ions with I^- ions in the precursor solution or post-synthesis anion-exchange.[20-23] Besides halide substitution, an additional level of control over intrinsic properties of all-inorganic perovskites is to introduce dopants. Impurity doping that incorporates appropriate ions into host lattices, for example, Mn^{2+}, has been demonstrated as an effective approach to modulate the electronic and optical properties of II-VI semiconductor nanocrystals.[24-26] Motivated by these novel functionalities, recently, several works have demonstrated that Mn^{2+} ions can also be introduced into the lattices of $CsPbX_3$ nanocrystals by using a modified synthetic method.[27-44] Intriguingly, the Mn-doped $CsPbCl_3$ created electronic state in the midgap region of $CsPbCl_3$ and displayed distinct charge transfer

dynamics.[32-34,40-41] Additionally, it was possible to tune the optical and electronic properties of $CsPbX_3$ nanocrystals by controlling the concentration of Mn^{2+} ions or synthetic temperature.[37] However, almost all of these works focused on Mn-doped $CsPbCl_3$ nanocrystals, which were unsuitable for the photovoltaic applications due to their large bandgaps.

Here, we successfully synthesized novel Mn-doped all-inorganic perovskites, $CsPb_{1-x}Mn_xI_{1+2x}Br_{2-2x}$, in ambient atmosphere without any control of humidity. Note that in this work, MnI_2 is used to replace $PbBr_2$ in the $CsPbIBr_2$ precursor solution, therefore when the Mn doping concentration is varied, a correlated change ~~only~~ also takes place for the I:Br ratio, which may also play a minor role in the increased performance. As the concentration of Mn^{2+} ions increased, the bandgaps of $CsPb_{1-x}Mn_xI_{1+2x}Br_{2-2x}$ could be reduced from 1.89 eV to 1.75 eV. Moreover, when the concentration of Mn dopants was appropriate, this novel Mn-doped all-inorganic perovskite film showed better crystallinity and morphology than the undoped counterpart. We employed these novel Mn-doped all-inorganic perovskite films into the all-inorganic PSCs with the simple structure of fluorine doped tin oxide (FTO)/compact TiO_2 (c-TiO_2)/mesoporous TiO_2 (m-TiO_2)/$CsPb_{1-x}Mn_xI_{1+2x}Br_{2-2x}$/Carbon, which displayed better photovoltaic performance than the $CsPbIBr_2$ film. Equally important, the encapsulated PSCs based on $CsPb_{0.995}Mn_{0.005}I_{1.01}Br_{1.99}$ showed good stability in ambient atmosphere.

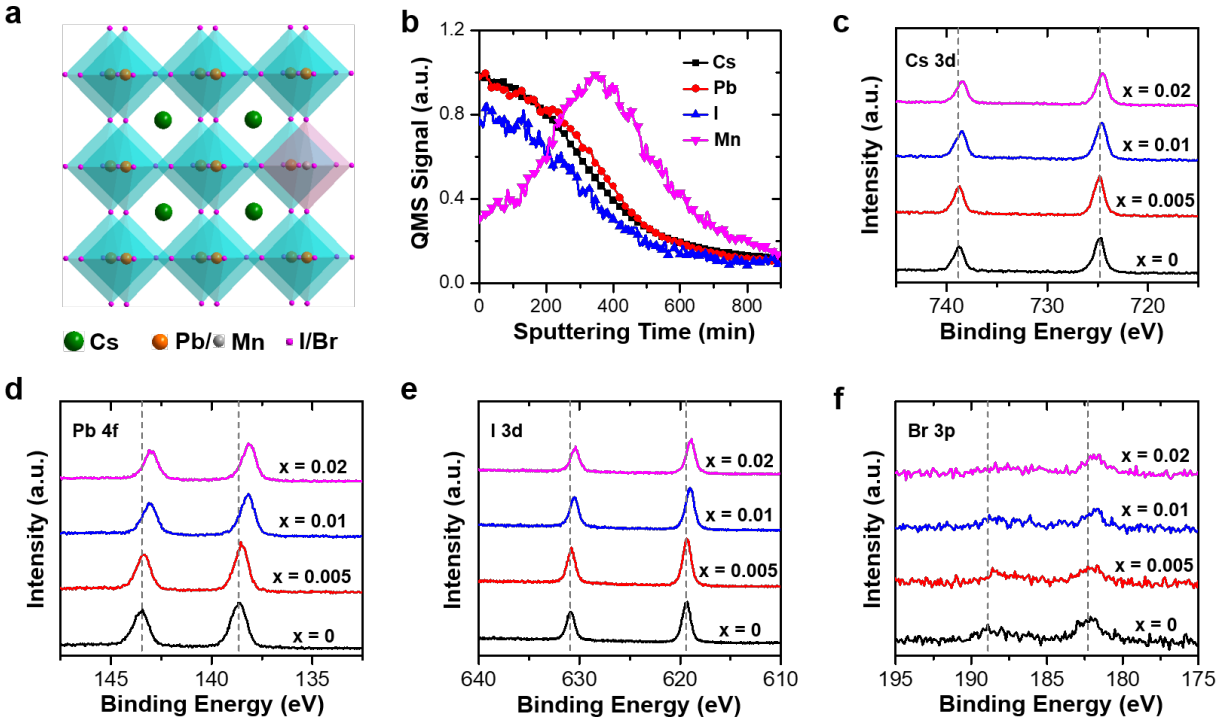

Figure 1 (a) Typical crystal structure of Mn-doped all-inorganic perovskite $CsPbIBr_2$ (labeled as $CsPb_{1-x}Mn_xI_{1+2x}Br_{2-2x}$), where Mn is placed in the position of Pb. (b) SIMS depth profile of $CsPb_{0.995}Mn_{0.005}I_{1.01}Br_{1.99}$ film for Cs, Pb, I, and Mn elements. High-resolution XPS spectra of $CsPbIBr_2$ (x = 0) and $CsPb_{1-x}Mn_xI_{1+2x}Br_{2-2x}$ (x = 0.005, 0.01, and 0.02) films at the (c) Cs 3d, (d) Pb 4f, (e) I 3d and (f) Br 3p regions, respectively~~(From bottom to top, there are $CsPbIBr_2$, $CsPb_{0.995}Mn_{0.005}I_{1.01}Br_{1.99}$, $CsPb_{0.99}Mn_{0.01}I_{1.02}Br_{1.98}$, and $CsPb_{0.95}Mn_{0.05}I_{1.1}Br_{1.9}$)~~.

All-inorganic perovskite $CsPbIBr_2$ films doped with Mn^{2+} ions at different concentrations ($CsPb_{1-x}Mn_xI_{1+2x}Br_{2-2x}$ (x = 0.005, 0.01, and 0.02)) were prepared under ambient atmosphere after modifying the two-step solution method (see Methods for details). For $CsPbX_3$ and $CsMnX_3$ (X = Cl, Br, or I) crystals, because of the similar octahedral coordination environment composing with Pb (or Mn) cations and six halide and the big difference between Mn ions and Cs (or X ions) in radius and valence state, we speculate that the Mn ion dopants may prefer to occupy the position of Pb ions. **Figure 1a** shows the typical crystal structure of the new perovskites $CsPb_{1-x}Mn_xI_{1+2x}Br_{2-2x}$, where Mn is placed in the position of Pb. In order to identify the compositions and chemical states of $CsPbIBr_2$ and $CsPb_{1-x}Mn_xI_{1+2x}Br_{2-2x}$ (x = 0.005, 0.01, and 0.02) films, X-ray photoelectron spectroscopy (XPS)

measurements were performed, as shown in **Figure S1**. The Mn peaks were not found in $CsPb_{1-x}Mn_xI_{1+2x}Br_{2-2x}$ (x = 0.005, 0.01, and 0.02) films, which can be ascribed to the atomic percentage below the detection limits. Another possibility is that Mn dopants on the top surface migrate into the bulk film, and because the XPS measurement is surface sensitive, and can only usually detect the elements in the top surface up to approximately 10 nm into the bulk, the Mn signal is too weak to detect.[45] As an alternative way to detect Mn, we performed secondary ion mass spectroscopy (SIMS) depth profiling on the $CsPb_{0.995}Mn_{0.005}I_{1.01}Br_{1.99}$ film, as shown in **Figure 1b**, indicating that Mn^{2+} ions were inserted into the $CsPbIBr_2$ ~~lattices~~ films successfully. On the one hand, Mn ions may be inserted into the $CsPbIBr_2$ lattices and replace partial Pb ions. On the other hand, Mn ions may present in this film by absorbing at grain boundaries or as a separate amorphous or as small nanocrystalline. The SIMS result reveals the Mn distribution with a gradient showing a higher concentration under the surface, which supports our hypothesis. With the binding energy of C 1s set at 284.6 eV (**Figure S2**), the high-resolution XPS spectra for various elements (Cs 3d, Pb 4f, I 3d, and Br 3p) were shown in **Figure 1c-f**. Notably, a uniform shift of peak positions to lower binding energy was observed in $CsPb_{1-x}Mn_xI_{1+2x}Br_{2-2x}$ films for Cs 3d, Pb 4f, I 3d, and Br 3p. These shifts are correlated with the insertion of Mn^{2+} ions, ~~which evidences~~ evidencing the successful introduction of Mn dopants in $CsPbIBr_2$,which is in accordane with previous reports.[27-44] In theory, these shifts can be comprehended by the radius difference between Mn^{2+} and Pb^{2+} ions. Specifically, the Mn^{2+} ion (~0.97 Å) shows a smaller radius than the Pb^{2+} ion (~1.33 Å), leading to the contraction of the BX_6 (B = Pb or Mn; X = I or Br) octahedral volume, which leads to the changes of chemical bonding properties and is reflected by the shifts in XPS spectra.[27] Phase stability of perovskites is determined by the volumetric ratio between BX_6 octahedra and Cs cation.[46] The contraction of the BX_6 octahedra results in that better holding of the BX_6 octahedra by the Cs cation in the

perovskite structure more easily, leading to the enhancement of phase stability of $CsPb_{1-x}Mn_xI_{1+2x}Br_{2-2x}$ films.

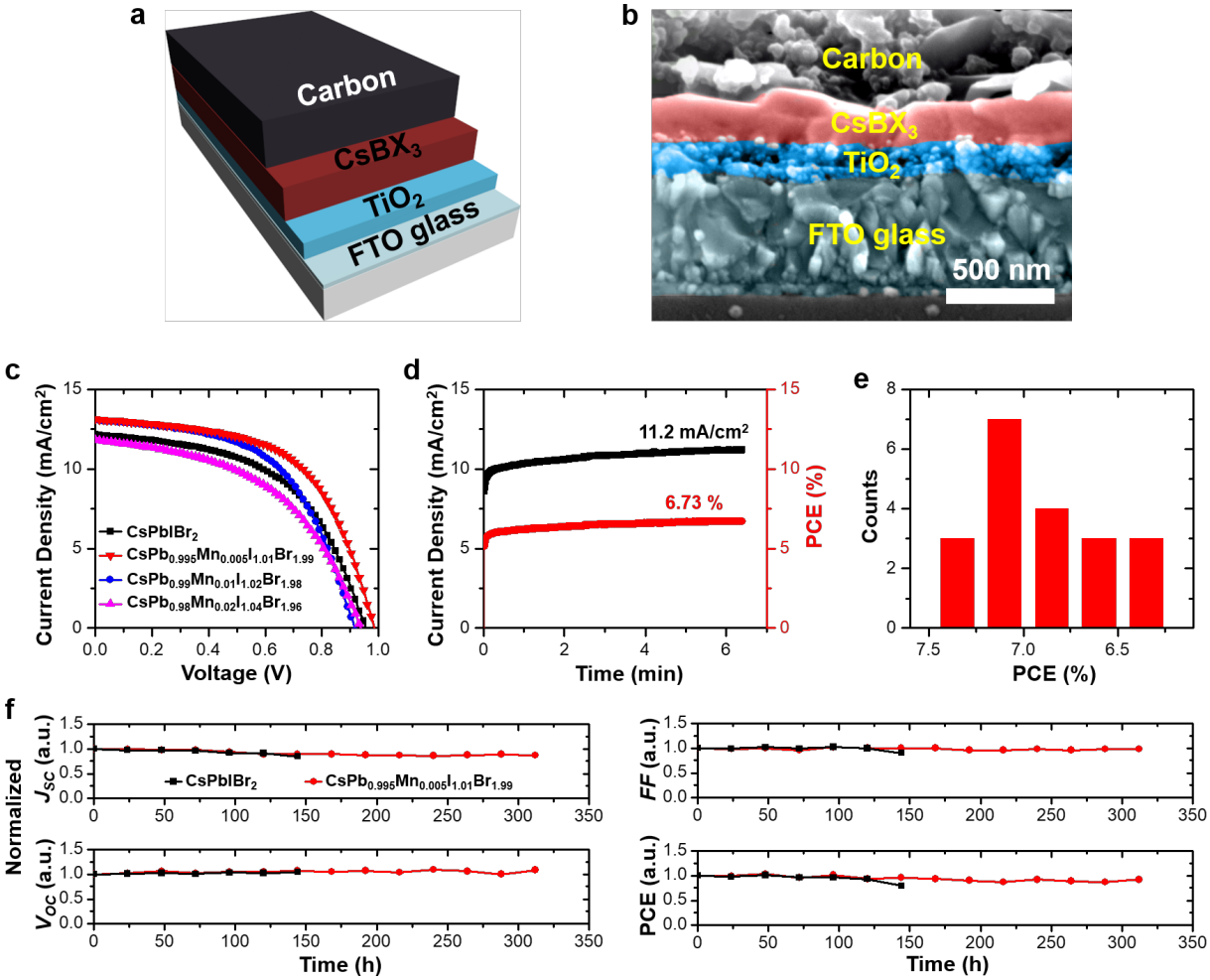

Figure 2 (a) Schematic diagram and (b) cross-sectional SEM image of all-inorganic PSCs with the structure of FTO/c-TiO_2/m-TiO_2/$CsBX_3$/Carbon. ~~(c) Energy level diagrams of all-inorganic PSCs. Mn^{2+} ions doping will result in the changes of CBM and VBM, which was displayed using yellow dash line.~~ (c) *J-V* curves of all-inorganic PSCs based on $CsPbIBr_2$ and $CsPb_{1-x}Mn_xI_{1+2x}Br_{2-2x}$ (x = 0.005, 0.01, and 0.02), respectively. (d) Current density and PCE as functions of time for the all-inorganic PSC based on $CsPb_{0.995}Mn_{0.005}I_{1.01}Br_{1.99}$. (e) Statistical histogram of PCEs obtained from 20 individual all-inorganic PSCs based on $CsPb_{0.995}Mn_{0.005}I_{1.01}Br_{1.99}$. (f) Normalized J_{SC}, V_{OC}, *FF* and PCE retentions of encapsulated all-inorganic PSCs based on $CsPbIBr_2$ and $CsPb_{0.995}Mn_{0.005}I_{1.01}Br_{1.99}$ under ambient atmosphere.

To confirm the effectiveness of Mn dopants on photovoltaic performances, all-inorganic PSCs with a simple structure of FTO/c-TiO_2/m-TiO_2/$CsBX_3$/Carbon were fabricated (**Figure 2a**). Clearly, all the organic components in the traditional organic-inorganic PSCs were completely eliminated, preventing the disadvantages caused by them, especially the cost to synthesize organic cations and the performance instability against heating. **Figure 2b** displays the cross-sectional SEM image of the all-inorganic PSCs based on $CsPb_{0.995}Mn_{0.005}I_{1.01}Br_{1.99}$, which depicts a uniform deposition. The thickness of the $CsPb_{0.995}Mn_{0.005}I_{1.01}Br_{1.99}$ is determined to be ~250 nm. **Figure S3** shows the energy band levels of all-inorganic PSCs, which reveals the electron extraction from the conduction band minimum (CBM) of $CsBX_3$ to that of TiO_2 and hole extraction from the valence band maximum (VBM) of $CsBX_3$ to that of the carbon electrode. In theory, for the $CsBX_3$ perovskite structure, the VBM is mainly composed of antibonding hybridization B 6s and X *n*p orbitals with dominant contributions from X *n*p, while the CBM is determined by antibonding mixing of B 6p and X *n*p orbitals, with major contribution from B 6p.[47] Therefore, Mn^{2+} ions doping can tune the band structure of $CsBX_3$, which is displayed temporarily using yellow dash lines in **Figure S3** and the detailed information can be found in the following part.

Figure 2c shows the current density-voltage (*J-V*) curves of all-inorganic PSCs based on $CsPbIBr_2$ and $CsPb_{1-x}Mn_xI_{1+2x}Br_{2-2x}$ (x = 0.005, 0.01, and 0.02), respectively. The corresponding photovoltaic parameters were summarized in **Table S1**. As a reference device, the all-inorganic PSCs based on $CsPbIBr_2$ revealed a PCE of 6.14%, which was comparable with the reported works.[20-23] For $CsPb_{1-x}Mn_xI_{1+2x}Br_{2-2x}$ (x = 0.005, 0.01, and 0.02), as the increase of the concentration of Mn^{2+} ions, the PCEs of all-inorganic PSCs based on them increased first and then decreased, reaching the highest PCE of 7.36% when x = 0.005. **Figure S4** shows the time-resolved photoluminescence (TR-PL) two-exponential decay curves of the $CsPb_{0.995}Mn_{0.005}I_{1.01}Br_{1.99}$ film with and without TiO_2 layer, respectively, which indicates electrons can transfer from $CsPb_{0.995}Mn_{0.005}I_{1.01}Br_{1.99}$ to TiO_2 effectively. Notably,

although the PCE of all-inorganic PSC based on $CsPb_{0.99}Mn_{0.01}I_{1.02}Br_{1.98}$ (x = 0.01) was lower than that based on $CsPb_{0.995}Mn_{0.005}I_{1.01}Br_{1.99}$ (x = 0.005), it was still higher than the all-inorganic PSC based on $CsPbIBr_2$, indicating that the Mn dopants were also effective in relatively high concentrations for achieving a higher performance. However, when the concentration of Mn dopants increased further to e.g., x = 0.02, the PCE of all-inorganic PSC decreased to 5.41%. This can be ascribed to changes of the $CsPb_{0.95}Mn_{0.05}I_{1.1}Br_{1.9}$ film on the electronic property, film crystalline, and film morphology, and the detailed discussion will be provided in the following part. The decreased performance also demonstrates that Mn^{2+} ion dopants play a more important role than that of I^- ion dopants, because if the effect of I^- ion incorporation is greater, incorporation of more I^- ion in the perovskite structure should result in an even higher performance.[20] **Figure 2d** displays the plots of current density and PCE as functions of time for the all-inorganic PSC based on $CsPb_{0.995}Mn_{0.005}I_{1.01}Br_{1.99}$, which reveals the current density and PCE of the all-inorganic PSC remain stable within 6 min under constant illumination. To demonstrate the reproducibility, 20 individual all-inorganic PSCs based on $CsPb_{0.995}Mn_{0.005}I_{1.01}Br_{1.99}$ were fabricated (**Figure 2e**). The statistical histogram shows that the PCE values of these 20 cells distributed over a narrow range with an average PCE of 7.0%, suggesting that $CsPb_{0.995}Mn_{0.005}I_{1.01}Br_{1.99}$ films with superior quality and homogeneous thickness can be prepared with high reproducibility using the preparation process described in this article. The long-term shelf-storage stability of all-inorganic PSCs based on $CsPbIBr_2$ and $CsPb_{0.995}Mn_{0.005}I_{1.01}Br_{1.99}$ was also measured, respectively. **Figure 2f** shows the time evolution of J_{SC}, V_{OC}, *FF*, and PCE for encapsulated all-inorganic PSCs in air. ~~Remarkably, t~~The encapsulated PSCs based on $CsPb_{0.995}Mn_{0.005}I_{1.01}Br_{1.99}$ revealed higher stability, showing little degradation (PCE decreased by 8% of the initial value) even after keeping for more than 300 hours in ambient atmosphere, while for encapsulated PSCs based on $CsPbIBr_2$, they decreased by 20% of the intial value just after ~ 144 hours.

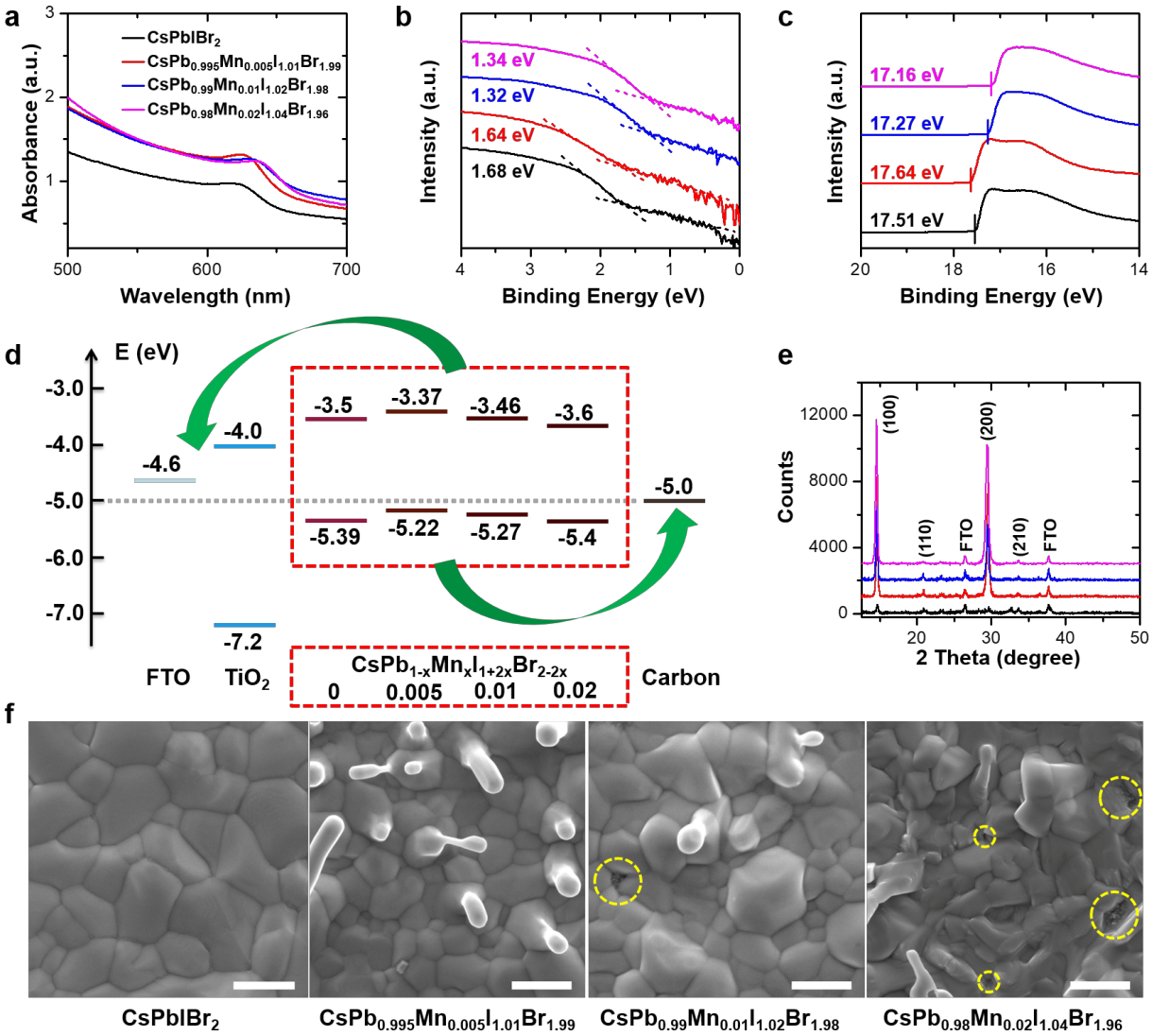

Figure 3 (a) UV-vis spectra, UPS spectra of (b) VBM onset and (c) photoemission cutoff energy boundary of $CsPbIBr_2$ and $CsPb_{1-x}Mn_xI_{1+2x}Br_{2-2x}$ perovskites (x = 0.005, 0.01, and 0.02), respectively. (d) Energy level diagram of FTO, TiO_2, $CsPbIBr_2$ (x = 0) and $CsPb_{1-x}Mn_xI_{1+2x}Br_{2-2x}$ perovskites (x = 0.005, 0.01, and 0.02), and carbon. The band structures for FTO, TiO_2, and carbon were referred by previous literature.[11,48-50] (e) XRD patterns, and (f) typical SEM images of $CsPbIBr_2$ and $CsPb_{1-x}Mn_xI_{1+2x}Br_{2-2x}$ (x = 0.005, 0.01, and 0.02) films, respectively. All the scale bars in Figure 3f are 1 μm. The areas marked by yellow dash circles are several pinholes.

To investigate the effect of Mn dopants in the all-inorganic perovskite $CsPbIBr_2$, we studied the optical and electronic properties of $CsPbIBr_2$ and $CsPb_{1-x}Mn_xI_{1+2x}Br_{2-2x}$ (x = 0.005, 0.01,

and 0.02) films, respectively. First, we measured the UV-vis spectra of $CsPbIBr_2$ and $CsPb_{1-x}Mn_xI_{1+2x}Br_{2-2x}$ (x = 0.005, 0.01, and 0.02) films, which are shown in **Figure 3a**. When Mn dopants were incorporated, clear red shifts were observed in $CsPb_{1-x}Mn_xI_{1+2x}Br_{2-2x}$ (x = 0.005, 0.01, and 0.02) films. Moreover, the absorbance intensities of these Mn-doped films became higher over the entire wavelength. **Figure S5** displays the transformed plots from the UV-vis absorption spectra, which reveal the bandgaps of the four kinds of perovskite films. The corresponding parameters were summarized in **Table S1**. As the Mn concentration increased, the bandgap became smaller and decreased to 1.80 eV for $CsPb_{1.98}Mn_{0.02}I_{1.04}Br_{1.96}$ film, which helps improved light harvesting. When we increased the Mn concentration, the bandgap would be further decreased to 1.75 eV, however, its photovoltaic performance in all-inorganic PSC became very low, as shown in **Figure S6 and Table S1**, which can be ascribed to its poor morphology (**Figure S7a**). In addition, the electronic structures of $CsPbIBr_2$ and $CsPb_{1-x}Mn_xI_{1+2x}Br_{2-2x}$ (x = 0.005, 0.01, and 0.02) films were investigated by ultraviolet photoelectron spectroscopy (UPS). **Figure 3b** and **c** display the UPS spectra of VBM onset and secondary electron cutoff energy boundary of $CsPbIBr_2$ (x = 0) and $CsPb_{1-x}Mn_xI_{1+2x}Br_{2-2x}$ films (x = 0.005, 0.01, and 0.02), respectively. According to the formula of VBM = 21.22 – ($E_{cutoff} – E_{onset}$), VBM energies of the four kinds of perovskite films were calculated to be 5.39, 5.22, 5.27, and 5.4 eV, respectively.[51-52] Combining the bandgaps obtained from UV-vis spectra, the ~~exactly~~ energy level diagrams were plotted, as shown in **Figure 3d**, in which the energy differences between VBMs of these perovskite films and carbon were determined to be 0.39, 0.22, 0.27, and 0.4 eV, respectively. The $CsPb_{0.995}Mn_{0.005}I_{1.01}Br_{1.99}$ film had the smallest energy difference, indicating that the energy loss for hole transfer from its VBM to carbon was the lowest among the four kinds of perovskite films.

Moreover, the crystallinities of $CsPbIBr_2$ and $CsPb_{1-x}Mn_xI_{1+2x}Br_{2-2x}$ (x = 0.005, 0.01, and 0.02) films were also studied to investigate the effect of Mn dopants in the all-inorganic perovskite $CsPbIBr_2$. X-Ray diffraction (XRD) patterns of the four kinds of perovskite films

are shown in **Figure 3e**. For $CsPbIBr_2$ film, besides two peaks from the FTO substrate, other identified XRD peaks could be indexed to the standard patterns of $CsPbIBr_2$ in the perovskite cubic phase.[20-23] When Mn dopants were incorporated, no additional phase could be observed, but the peak intensities became stronger, indicating better crystallinities for $CsPb_{1-x}Mn_xI_{1+2x}Br_{2-2x}$ (x = 0.005, 0.01, and 0.02) films. We propose that such enhanced crystallinity in the Mn-doped perovskite film could be cased by that the ~~was expected because~~ doping removed some of the pre-existing structural defects, leading to continuous charge-transport channels that enabled the highly mobile photo-generated carriers to travel in $CsPb_{1-x}Mn_xI_{1+2x}Br_{2-2x}$ (x = 0.005, 0.01, and 0.02) films.

Finally, to study the effect of Mn dopants on morphologies of $CsPbIBr_2$ and $CsPb_{1-x}Mn_xI_{1+2x}Br_{2-2x}$ (x = 0.005, 0.01, and 0.02) films, scanning electron microscope (SEM) images were performed, as shown in **Figure 3f**. As a reference sample, the $CsPbIBr_2$ film shows a smooth surface and consists of dense particles with an average grain size of ~1 μm. When the Mn dopants were incorporated, the morphology of $CsPb_{0.995}Mn_{0.005}I_{1.01}Br_{1.99}$ film underwent a dramatic change: vertical branches emerged on its surface (**Figure 3f**). These vertical branches are beneficial for the PSC device applications, because they will protrude into the carbon electrode to increase the contact area between perovskite and carbon, boosting hole transfer from perovskite to carbon electrode. However, when the concentration of Mn dopants was increased further (see SEM images for $CsPb_{0.99}Mn_{0.01}I_{1.02}Br_{1.98}$ and $CsPb_{0.98}Mn_{0.02}I_{1.04}Br_{1.96}$ in **Figure 3f**), the amount of vertical branches decreased and some pinholes appeared on the surface. These pinholes can result in the direct contact between TiO_2 and carbon in all-inorganic PSCs, increasing the charge recombination and decreasing the photovoltaic performance. We hypothesize that these pinholes stem from the severe contraction of the perovskite structure when more Mn dopants are incorporated (**Figure 1**). If our hypothesis is correct, more Mn dopants will result in severer contraction, and the perovskite structure will be destroyed when the concentration of Mn dopants is beyond the

threshold value. To demonstrate this prediction, we prepared $CsPb_{1-x}Mn_xI_{1+2x}Br_{2-2x}$ films with more Mn dopants. **Figure S7a** shows the typical SEM image of $CsPb_{0.95}Mn_{0.05}I_{1.1}Br_{1.9}$ (x = 0.05) film, which exhibits severer contraction than the $CsPb_{0.98}Mn_{0.02}I_{1.04}Br_{1.96}$ film. Moreover, due to the severe contraction in the structure, more defect states appear in this film and the intensity of XRD peaks become much lower (**Figure S7b**). However, because the amount of Mn dopants does not exceed the threshold value, this film still forms a perovskite structure (**Figure S7b**). When we further increased the Mn dopants concentration, such as, $CsPb_{0.8}Mn_{0.2}I_{1.4}Br_{1.6}$ (x = 0.2) film, we could not obtain a perovskite structure any more, as shown in **Figure S7b**, which indicated that the perovskite structure in $CsPb_{0.8}Mn_{0.2}I_{1.4}Br_{1.6}$ (x = 0.2) film was destroyed. Actually, in experiment, we just obtained a yellow non-perovskite film when x = 0.2. In short, the doping concentration is important for the morphology of the Mn-doped perovskite film. The appropriate doping concentration can optimize the morphology for the application of PSCs, however, the excessive doping concentration can damage the morphology and destroy the perovskite structure.

In summary, novel Mn-doped all-inorganic perovskites, $CsPb_{1-x}Mn_xI_{1+2x}Br_{2-2x}$, were prepared using two-step solution-phase method in ambient atmosphere without any control of humidity. By eliminating the organic components completely, all-inorganic PSCs based on $CsPb_{1-x}Mn_xI_{1+2x}Br_{2-2x}$ films were fabricated. When the doping concentration was appropriate (x = 0.005), the all-inorganic PSC based on $CsPb_{0.995}Mn_{0.005}I_{1.01}Br_{1.99}$ film displayed the highest PCE. This enhancement first could be ascribed to small bandgap and ideal band structure of the $CsPb_{0.995}Mn_{0.005}I_{1.01}Br_{1.99}$ film, which improved the light harvesting ability and reduce energy loss in hole transfer. In addition, when appropriate Mn dopant concentration was introduced, the $CsPb_{0.995}Mn_{0.005}I_{1.01}Br_{1.99}$ film exhibited better crystallinity and morphology, providing a smooth path for charge-transfer in PSCs. The analyses presented here not only reveal the underlying factors contributing to the photovoltaic properties of the

Mn-doped perovskite, but also open the door for further studies on other dopants in perovskite materials.

Supporting Information
Supporting Information is available from the Wiley Online Library or from the author.

Acknowledgements
J. Liang and Z. H. Liu contributed equally to this work. This work was supported by funding from the Energy Materials and Surface Sciences Unit of the Okinawa Institute of Science and Technology Graduate University, the OIST R&D Cluster Research Program, and the OIST Proof of Concept (POC) Program. Dr. J. Liang would like to thank the Peter M. and Ruth L. Nicholas Postdoctoral Fellowship from the Smalley-Curl Institute for Nanoscale Science and Technology for the financial support. The authors also would like to thank Dr. Mikas Remeika for writing the software for steady-state power measurements.

Received: ((will be filled in by the editorial staff))
Revised: ((will be filled in by the editorial staff))
Published online: ((will be filled in by the editorial staff))

References

[1] J. Burschka, N. Pellet, S. J. Moon, R. Humphry-Baker, P. Gao, M. K. Nazeeruddin and M. Gratzel, *Nature*, **2013**, *499*, 316.

[2] M. Z. Liu, M. B. Johnston and H. J. Snaith, *Nature*, **2013**, *501*, 395.

[3] A. Y. Mei, X. Li, L. F. Liu, Z. L. Ku, T. F. Liu, Y. G. Rong, M. Xu, M. Hu, J. Z. Chen, Y. Yang, M. Gratzel and H. W. Han, *Science*, **2014**, *345*, 295.

[4] H. P. Zhou, Q. Chen, G. Li, S. Luo, T. B. Song, H. S. Duan, Z. R. Hong, J. B. You, Y. S. Liu and Y. Yang, *Science*, **2014**, *345*, 542.

[5] L. K. Ono, N. G. Park, K. Zhu, W. Huang, Y. B. Qi, *ACS Energy Lett.* **2017**, *2*, 1749.

[6] L. K. Ono, E. J. Juárez-Pérez, Y. B. Qi, *ACS Appl. Mater. Interfaces* **2017,** *9*, 30197.

[7] L. K. Ono, Y. B. Qi, *J. Phys. D Appl. Phys.* **2018**, *51*, 9.

[8] N. J. Jeon, J. H. Noh, W. S. Yang, Y. C. Kim, S. Ryu, J. Seo and S. I. Seok, *Nature*, **2015**, *517*, 476.

[9] M. Saliba, T. Matsui, K. Domanski, J. Y. Seo, A. Ummadisingu, S. M. Zakeeruddin, J. P. Correa-Baena, W. R. Tress, A. Abate, A. Hagfeldt and M. Gratzel, *Science*, **2016**, *354*, 206-209.

[10] W. Ahmad, J. Khan, G. D. Niu and J. Tang, *Solar RRL*, **2017**, *1*, 1700048.

[11] J. Liang, C. X. Wang, Y. R. Wang, Z. R. Xu, Z. P. Lu, Y. Ma, H. F. Zhu, Y. Hu, C. C. Xiao, X. Yi, G. Y. Zhu, H. L. Lv, L. B. Ma, T. Chen, Z. X. Tie, Z. Jin and J. Liu, *J. Am. Chem. Soc.*, **2016**, *138*, 15829.

[12] X. W. Chang, W. P. Li, L. Q. Zhu, H. C. Liu, H. F. Geng, S. S. Xiang, J. M. Liu and H. N. Chen, *ACS Appl. Mater. Interfaces*, **2016**, *8*, 33649.

[13] A. Swarnkar, A. R. Marshall, E. M. Sanehira, B. D. Chernomordik, D. T. Moore, J. A. Christians, T. Chakrabarti and J. M. Luther, *Science*, **2016**, *354*, 92.

[14] M. Kulbak, D. Cahen and G. Hodes, *J. Phys. Chem. Lett.*, **2015**, *6*, 2452.

[15] M. Kulbak, S. Gupta, N. Kedem, I. Levine, T. Bendikov, G. Hodes and D. Cahen, *J. Phys. Chem. Lett.*, **2016**, *7*, 167.

[16] J. Liang, J. Liu and Z. Jin, *Solar RRL*, **2017**, *1*, 1700086.

[17] L. B. Qiu, L. K. Ono, Y. B. Qi, Advances and challenges to the commercialization of organic–inorganic halide perovskite solar cell technology. *Mater. Today Energy* **2017**, *7*, 169.

[18] L. K. Ono, M. R. Leyden, S. H. Wang, Y. B. Qi, Organometal Halide Perovskite Thin Films and Solar Cells by Vapor Deposition. *J. Mater. Chem. A* **2016**, *4*, 6693.

[19] https://www.nrel.gov/pv/assets/images/efficiency-chart.png.

[20] R. J. Sutton, G. E. Eperon, L. Miranda, E. S. Parrott, B. A. Kamino, J. B. Patel, M. T. Horantner, M. B. Johnston, A. A. Haghighirad, D. T. Moore and H. J. Snaith, *Adv. Energy Mater.*, **2016**, *6*, 1502458.

[21] Q. S. Ma, S. J. Huang, X. M. Wen, M. A. Green and A. W. Y. Ho-Baillie, *Adv. Energy Mater.*, **2016**, *6*, 1502202.

[22] R. E. Beal, D. J. Slotcavage, T. Leijtens, A. R. Bowring, R. A. Belisle, W. H. Nguyen, G. F. Burkhard, E. T. Hoke and M. D. McGehee, *J. Phys. Chem. Lett.*, **2016**, *7*, 746.

[23] C. F. J. Lau, X. F. Deng, Q. S. Ma, J. H. Zheng, J. S. Yun, M. A. Green, S. J. Huang and A. W. Y. Ho-Baillie, *ACS Energy Lett.*, **2016**, *1*, 573.

[24] A. Nag, R. Cherian, P. Mahadevan, A. V. Gopal, A. Hazarika, A. Mohan, A. S. Vengurlekar and D. D. Sarma, *J. Phys. Chem. C*, **2010**, *114*, 18323

[25] D. J. Norris, A. L. Efros and S. C. Erwin, *Science*, **2008**, *319*, 1776.

[26] N. S. Karan, D. D. Sarma, R. M. Kadam and N. Pradhan, *J. Phys. Chem. Lett.*, 2010, 1, 2863.

[27] S. H. Zou, Y. S. Liu, J. H. Li, C. P. Liu, R. Feng, F. L. Jiang, Y. X. Li, J. Z. Song, H. B. Zeng, M. C. Hong and X. Y. Chen, *J. Am. Chem. Soc.*, **2017**, *139*, 11443.

[28] D. Q. Chen, G. L. Fang and X. Chen, *ACS Appl. Mater. Interfaces*, **2017**, *9*, 40477.

[29] C. K. Zhou, Y. Tian, O. Khabou, M. Worku, Y. Zhou, J. Hurley, H. R. Lin and B. W. Ma, *ACS Appl. Mater. Interfaces*, **2017**, *9*, 40446.

[30] Q. A. Akkerman, D. Meggiolaro, Z. Y. Dang, F. De Angelis and L. Manna, *ACS Energy Lett.*, **2017**, *2*, 2183.

[31] H. W. Liu, Z. N. Wu, J. R. Shao, D. Yao, H. Gao, Y. Liu, W. L. Yu, H. Zhang and B. Yang, *ACS Nano*, **2017**, *11*, 2239.

[32] A. K. Guria, S. K. Dutta, S. Das Adhikari and N. Pradhan, *ACS Energy Lett.*, **2017**, *2*, 1014.

[33] G. G. Huang, C. L. Wang, S. H. Xu, S. F. Zong, J. Lu, Z. Y. Wang, C. G. Lu and Y. P. Cui, *Adv. Mater.*, **2017**, *29*, 1700095.

[34] W. J. Mir, M. Jagadeeswararao, S. Das and A. Nag, *ACS Energy Lett.*, **2017**, *2*, 537.

[35] W. Xu, F. M. Li, F. Y. Lin, Y. Chen, Z. X. Cai, Y. R. Wang and X. Chen, *Adv. Optical Mater.*, **2017**, *5*, 1700520.

[36] A. Biswas, R. Bakthavatsalam and J. Kundu, *Chem. Mater.*, **2017**, *29*, 7816.

[37] X. Yuan, S. H. Ji, M. C. De Siena, L. L. Fei, Z. Zhao, Y. J. Wang, H. B. Li, J. L. Zhao and D. R. Gamelin, *Chem. Mater.*, 2017, 29, 8003.

[38] D. Rossi, D. Parobek, Y. T. Dong and D. H. Son, *J. Phys. Chem. C*, **2017**, *121*, 17143.

[39] P. Arunkumar, K. H. Gil, S. Won, S. Unithrattil, Y. H. Kim, H. J. Kim and W. B. Im, , *J. Phys. Chem. Lett.*, **2017**, *8*, 4161.

[40] W. Y. Liu, Q. L. Lin, H. B. Li, K. F. Wu, I. Robel, J. M. Pietryga and V. I. Klimov, *J. Am. Chem. Soc.*, **2016**, *138*, 14954.

[41] P. K. Santra and P. V. Kamat, *J. Am. Chem. Soc.*, **2012**, *134*, 2508.

[42] J. R. Zhu, X. L. Yang, Y. H. Zhu, Y. W. Wang, J. Cai, J. H. Shen, L. Y. Sun and C. Z. Li, *J. Phys. Chem. Lett.*, **2017**, *8*, 4167.

[43] D. Parobek, B. J. Roman, Y. T. Dong, H. Jin, E. Lee, M. Sheldon and D. H. Son, *Nano Lett.*, **2016**, *16*, 7376.

[44] C. C. Lin, K. Y. Xu, D. Wang and A. Meijerink, *Sci. Rep.*, **2017**, *7*, 45906.

[45] H. Hantsche, *Scanning* **2017,** *11*, 257.

[46] Z. Li, M. J. Yang, J. S. Park, S. H. Wei, J. J. Berry and K. Zhu, *Chem. Mater.*, **2016**, *28*, 284.

[47] R. E. Brandt, V. Stevanovic, D. S. Ginley and T. Buonassisi, *MRS Commun.*, **2015**, *5*, 265.

[48] Y. Hu, S. Si, A. Mei, Y. Rong, H. Liu, X. Li, H. W. Han, *Solar RRL*, **2017**, *1*, 1600019.

[49] Z. L. Ku, Y. G. Rong, M. Xu, T. F. Liu, H. W. Han, *Sci. Rep.* **2013**, *3*, 3132.

[50] Y. Xiong, X. Zhu, A. Mei, F. Qin, S. Liu, S. Zhang, Y. Jiang, Y. Zhou, H. W. Han, *Solar RRL*, **2018**, *2*, DOI: 10.1002/solr.201800002.

[51] Z. B. Yang, A. Rajagopal and A. K. Y. Jen, *Adv. Mater.*, **2017**, *29*, 1704418.

[52] Y. Hou, X. Y. Du, S. Scheiner, D. P. McMeekin, Z. P. Wang, N. Li, M. S. Killian, H. W. Chen, M. Richter, I. Levchuk, N. Schrenker, E. Spiecker, T. Stubhan, N. A. Luechinger, A.

Hirsch, P. Schmuki, H. P. Steinruck, R. H. Fink, M. Halik, H. J. Snaith and C. J. Brabec, *Science*, **2017**, *358*, 1192.

Short summary:

All-inorganic perovskite materials have great potential in realizing long term stability in perovskite solar cells (PSCs). In this work Prof. Yabing Qi and co-workers from Okinawa Institute of Science and Technology Graduate University developed a method to dope all-inorganic perovskite $CsPbIBr_2$ with Mn. PSCs fabricated based on the Mn-doped $CsPbIBr_2$ using low-cost carbon electrodes show substantially improved efficiency and stability.

doping, Mn, all-inorganic perovskite, perovskite solar cell, carbon electrode

J. Liang, Z. H. Liu, L. B. Qiu, Z. Hawash, L. Q. Meng, Z. F. Wu, Y. Jiang, L. K. Ono and Y. B. Qi*

Enhancing Optical, Electronic, Crystalline, and Morphological Properties of Cesium Lead Halide by Mn Substitution for High-Stability All-Inorganic Perovskite Solar Cells with Carbon Electrodes

TOC figure

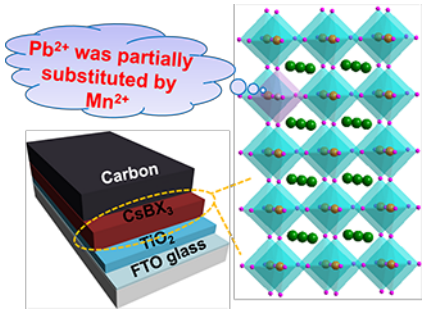

Supporting Information

Enhancing Optical, Electronic, Crystalline, and Morphological Properties of Cesium Lead Halide by Mn Substitution for High-Stability All-Inorganic Perovskite Solar Cells with Carbon Electrodes

*Jia Liang, Zonghao Liu, Longbin Qiu, Zafer Hawash, Lingqiang Meng, Zhifang Wu, Yan Jiang, Luis K. Ono and Yabing Qi**

Supporting Information

Enhancing Optical, Electronic, Crystalline, and Morphological Properties of Cesium Lead Halide by Mn Substitution for High-Stability All-Inorganic Perovskite Solar Cells with Carbon Electrodes

*Jia Liang, Zonghao Liu, Longbin Qiu, Zafer Hawash, Lingqiang Meng, Zhifang Wu, Yan Jiang, Luis K. Ono and Yabing Qi**

Dr. J. Liang, Dr. Z. Liu, Dr. L. Qiu, Dr. Z. Hawash, Dr. L. Meng, Dr. Z. Wu, Dr. Y. Jiang, D. L. Ono, Prof. Y. Qi
Energy Materials and Surface Sciences Unit (EMSSU)
Okinawa Institute of Science and Technology Graduate University (OIST)
1919-1 Tancha, Onna-son, Kunigami-gun, Okinawa 904-0495, Japan
E-mail: Yabing.Qi@OIST.jp
Dr. J. Liang
Department of Materials Science and NanoEngineering/Smalley-Curl Institute
Rice University
Houston, Texas 77005, USA

Keywords: doping, Mn, all-inorganic perovskite, perovskite solar cell, carbon electrode

Methods

Preparation of all-inorganic PSCs

Fluorine-doped tin oxide (FTO)-coated glasses were washed sequentially with detergent, ethanol, and acetone with ultrasonication for 30 min each, and then they were dried by nitrogen and treated by plasma for 15 min. The c-TiO_2 layer was first deposited on FTO substrate by spin-coating an ethanol solution of titanium isopropoxide and diethanol amine at 7000 rpm for 30s, and then the FTO/c-TiO_2 substrate was annealed at 500 ℃ for 2 h in air. Following, the m-TiO_2 layer was deposited on FTO/c-TiO_2 substrate by spin-coating a mixture of 18NR-T TiO_2 paste and ethanol 1:8 (w/w) at 5000 rpm for 30s, and then sintered at 500 ℃ for 30 min in air again.

Subsequently, the $CsPbIBr_2$ and $CsPb_{1-x}Mn_xI_{1+2x}Br_{2-2x}$ (x = 0.005, 0.01, and 0.02) perovskite films were deposited on the FTO/c-TiO_2/m-TiO_2 substrate using a two-step solution deposition method in air without any control of humidity. Typically, 1-x mmol PbI_2 and x mmol MnI_2 (x = 0, 0.005, 0.01, and 0.02) were dissolved in dimethylformamide (DMF) to yield a 1 M solution under stirring at 80 °C for 30 min. Then, the mixture solution was deposited on the FTO/c-TiO_2/m-TiO_2 substrate by spin-coating at 2000 rpm for 30 s, followed by drying at 80 °C for 30 min. Then, the FTO/c-TiO_2/m-TiO_2/PbI_2 substrate was dipped into a methanol solution of 15 mg/mL CsBr for 10 min, washed with isopropoxide, dried by nitrogen, and heated at 350 ℃ for 45 s in air. After this procedure, the obtained $CsPbIBr_2$ (x = 0) and $CsPb_{1-x}Mn_xI_{1+2x}Br_{2-2x}$ (x = 0.005, 0.01, and 0.02) perovskite films were transferred into the glovebox. Finally, the carbon electrodes were prepared by doctor-blade coating conductive carbon ink on them using adhesive tapes as spaces, and then heated at 80 °C for 60 min.

Characterizations

In order to obtain the top surface and cross-section morphologies of the $CsPbIBr_2$ (x = 0) and $CsPb_{1-x}Mn_xI_{1+2x}Br_{2-2x}$ (x = 0.005, 0.01, and 0.02) perovskite films, scanning electron microscope was employed (SEM, Helios NanoLab G3 UC, FEI). The crystallinities of these perovskite films were measured using an X-ray diffractometer (D8 Discover, Bruker). To investigate the components of the perovskite $CsPbBr_3$, X-ray photoelectron spectroscopy (XPS) was performed with an Al Kα (1486.6 eV) X-ray source (Axis Ultra, KRATOS). The work function and the valence band position of $CsPbIBr_2$ (x = 0) and $CsPb_{1-x}Mn_xI_{1+2x}Br_{2-2x}$ (x = 0.005, 0.01, and 0.02) perovskite films were determined by ultraviolet photoemission spectroscopy (UPS) using a He I (21.22 eV) source. Chamber pressure was below 6.0E-9 Torr for XPS and UPS measurements. SIMS instrumentation (Kratos Axis ULTRA) is equipped with a quadrupole mass spectrometer (HAL 7, Hidden Analytical) and an ion sputter gun (IG20, Hiden Analytical). SIMS data was collected in the positive ion detection mode employing 1 keV Ar^+ primary beam with a 50 nA beam current and a diameter of 100 um. The beam was at an angle of 45° with respect to the sample surface normal. The base pressure of the Kratos system is maintained at low 10^{-9} Torr. The absorption spectra of the films were measured using a UV-visible spectrophotometer (JASCO Inc., V-670). The current density-voltage (*J-V*) curves and steady-state power output characteristics were measured under AM 1.5G illumination using a solar simulator (Newport Oriel Sol AAA) with a 2400 Source Meter (Keithley, U.S.A.). The light intensity was calibrated with a Si solar cell for 1 sun. Typically, in this study, the active area of the PSCs was 0.09 cm^2 and the scan rate was 0.1 V/s.

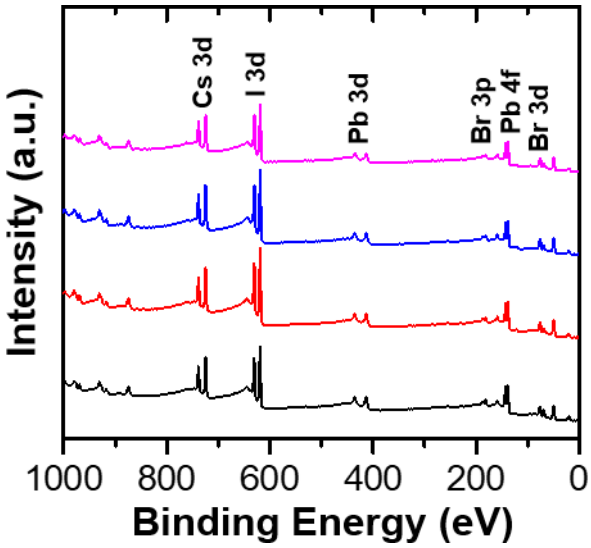

Figure S1 XPS survey spectra of $CsPbIBr_2$ and $CsPb_{1-x}Mn_xI_{1+2x}Br_{2-2x}$ inorganic perovskites (x = 0.005, 0.01, and 0.02), respectively. The spectra, from bottom to top, are $CsPbIBr_2$, $CsPb_{0.995}Mn_{0.005}I_{1.01}Br_{1.99}$, $CsPb_{0.99}Mn_{0.01}I_{1.02}Br_{1.98}$, and $CsPb_{0.98}Mn_{0.02}I_{1.04}Br_{1.96}$, respectively.

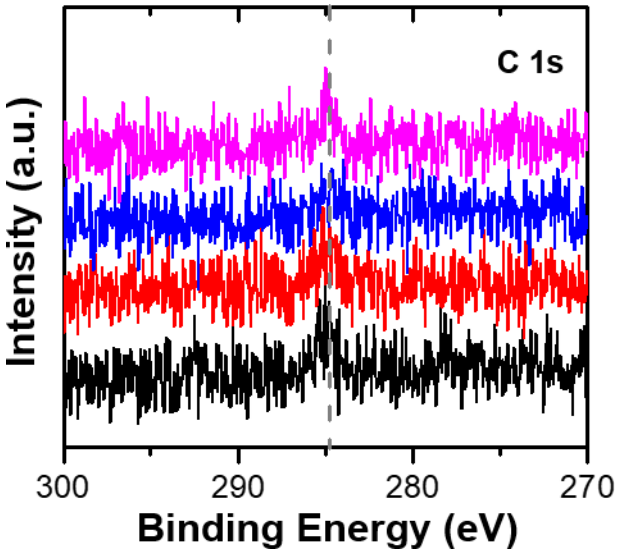

Figure S2 High-resolution XPS spectra of $CsPbIBr_2$ and $CsPb_{1-x}Mn_xI_{1+2x}Br_{2-2x}$ inorganic perovskites (x = 0.005, 0.01, and 0.02) at the C 1s region, respectively. The spectra, from bottom to top, are $CsPbIBr_2$, $CsPb_{0.995}Mn_{0.005}I_{1.01}Br_{1.99}$, $CsPb_{0.99}Mn_{0.01}I_{1.02}Br_{1.98}$, and $CsPb_{0.98}Mn_{0.02}I_{1.04}Br_{1.96}$, respectively.

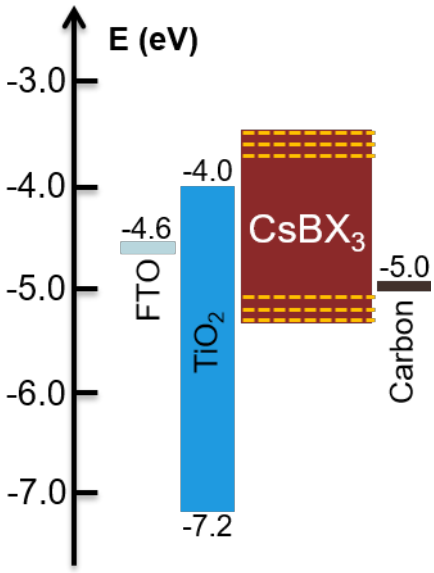

Figure S3 Energy level diagrams of all-inorganic PSCs. Mn^{2+} ions doping may result in the changes of CBM and / or VBM, which are displayed using yellow dash lines.

Table S1 Photovoltaic parameters and bandgaps of all-inorganic PSCs based on $CsPbIBr_2$ and $CsPb_{1-x}Mn_xI_{1+2x}Br_{2-2x}$ (x = 0.005, 0.01, and 0.02) films, respectively.

Samples	J_{SC} (mA/cm^2)	V_{OC} (V)	*FF*	PCE (%)	Bandgap (eV)
$CsPbIBr_2$	12.15	0.96	0.53	6.14	1.89
$CsPb_{0.995}Mn_{0.005}I_{1.01}Br_{1.99}$	13.15	0.99	0.57	7.36	1.85
$CsPb_{0.99}Mn_{0.01}I_{1.02}Br_{1.98}$	13.07	0.92	0.55	6.54	1.81
$CsPb_{0.98}Mn_{0.02}I_{1.04}Br_{1.96}$	11.86	0.95	0.49	5.41	1.80
$CsPb_{0.95}Mn_{0.05}I_{1.1}Br_{1.9}$	3.06	0.78	0.34	0.80	1.75

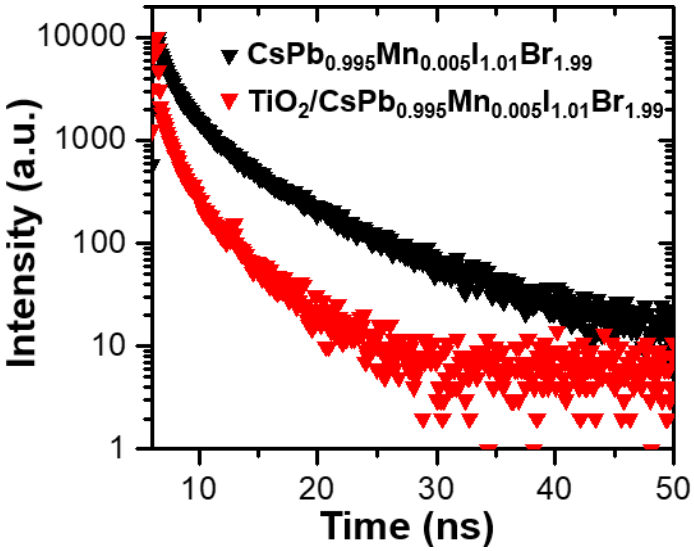

Figure S4 Time-resolved PL decay profiles of $CsPb_{0.995}Mn_{0.005}I_{1.01}Br_{1.99}$ films with and without a TiO_2 layer.

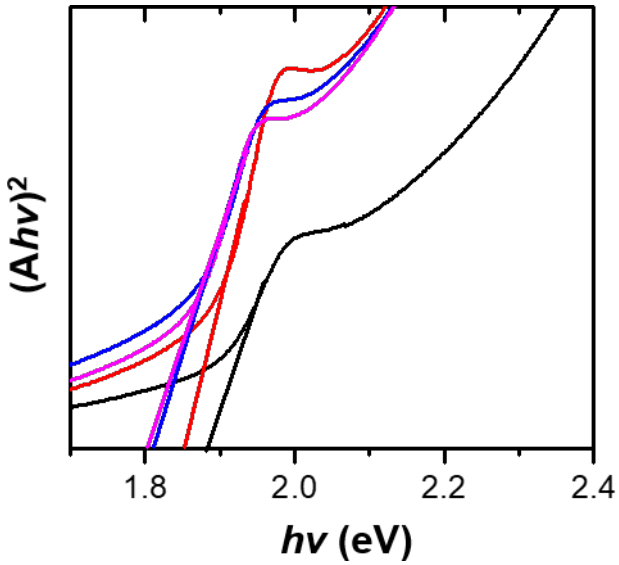

Figure S5 (A$h\nu$)^2-$h\nu$ curves of $CsPbIBr_2$ and $CsPb_{1-x}Mn_xI_{1+2x}Br_{2-2x}$ (x = 0.005, 0.01, and 0.02) films, respectively.

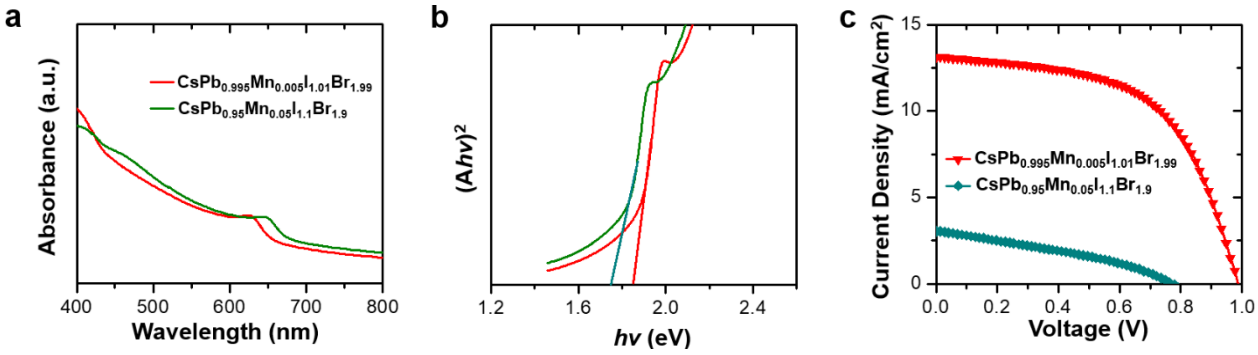

Figure S6 (a) UV-vis spectra and (b) $(Ahv)^2$-hv curves of $CsPb_{0.995}Mn_{0.005}I_{1.01}Br_{1.99}$ and $CsPb_{0.95}Mn_{0.05}I_{1.1}Br_{1.9}$ films, respectively. (c) *J-V* curves of all-inorganic PSCs based on $CsPb_{0.995}Mn_{0.005}I_{1.01}Br_{1.99}$ and $CsPb_{0.95}Mn_{0.05}I_{1.1}Br_{1.9}$ films, respectively.

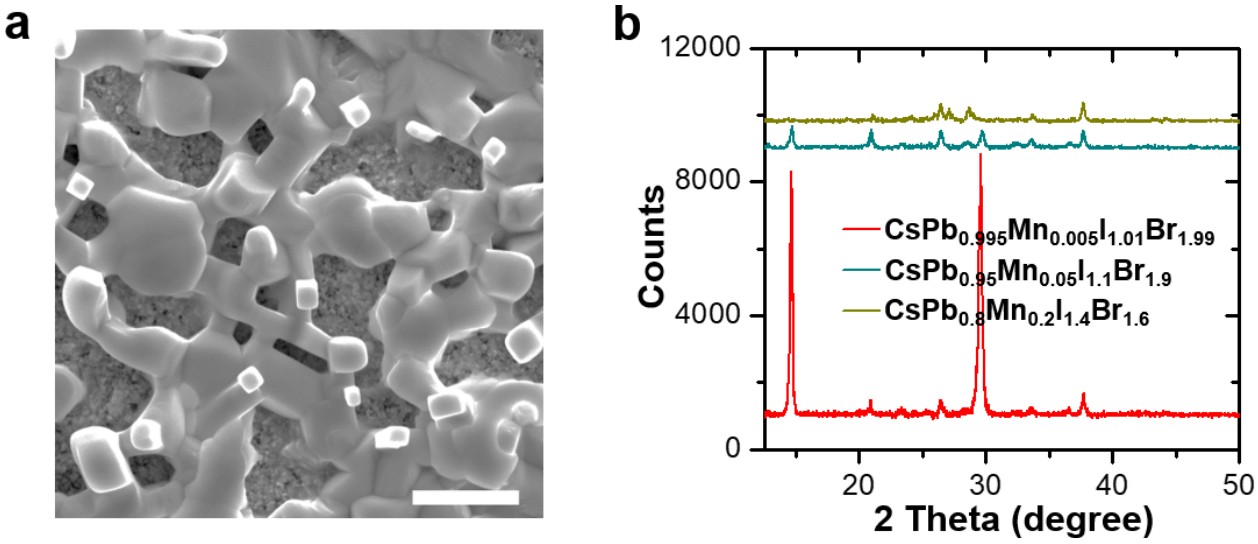

Figure S7 (a) Typical SEM image of $CsPb_{0.95}Mn_{0.05}I_{1.1}Br_{1.9}$ film; (b) XRD patterns of $CsPb_{0.995}Mn_{0.005}I_{1.01}Br_{1.99}$, $CsPb_{0.95}Mn_{0.05}I_{1.1}Br_{1.9}$, and $CsPb_{0.8}Mn_{0.2}I_{1.4}Br_{1.6}$ films, respectively.